

Spatial modeling of extremes and an angular component

G. Tamagny and M. Ribatet

Nantes Université, École Centrale Nantes, CNRS, Laboratoire de Mathématiques Jean Leray, LMJL, UMR 6629, F-44000 Nantes, France

Abstract

Many environmental processes such as rainfall, wind or snowfall are inherently spatial and the modelling of extremes has to take into account that feature. In addition, environmental processes are often attached with an angle, e.g., wind speed and direction or extreme snowfall and time of occurrence in year. This article proposes a Bayesian hierarchical model with a conditional independence assumption that aims at modelling simultaneously spatial extremes and an angular component. The proposed model relies on the extreme value theory as well as recent developments for handling directional statistics over a continuous domain. Working within a Bayesian setting, a Gibbs sampler is introduced whose performances are analysed through a simulation study. The paper ends with an application on extreme wind speed in France. Results show that extreme wind events in France are mainly coming from West apart from the Mediterranean part of France and the Alps.

Keywords: Extreme value theory, Spatial extremes, Circular statistics, Bayesian hierarchical models, Markov Chain Monte Carlo, Environmental application

1 Introduction

The accurate modelling of environmental extremes such as floods or heatwaves is crucial as they can lead to severe damages or economic losses. As a consequence, the last decade has seen many theoretical developments as well as extensive applications to try to analyse spatial extremes. From a probabilistic point of view, the relevant framework for modelling extreme events is the extreme value theory whose focus is precisely on the tail of the distribution.

In a spatial setting, Bayesian hierarchical models or max-stable and Pareto processes (???) are popular choices. While the latter approaches are relevant for modelling areal quantities as cumulative rainfall amount over a spatial domain, pointwise predictions of extremes is still of interest in many applications, e.g., design of dykes for floods. In this context, Bayesian hierarchical models have been found to be a very competitive choice and widely applicable as opposed to max-stable or Pareto processes for which inference is challenging and pointwise prediction less accurate (Dombry et al., 2017; Huser et al., 2019; Davison et al., 2012). As a consequence and, as long as pointwise prediction is of concern, one can restrict our attention to the univariate case for which extreme value theory justifies the use of the Generalized Extreme Value distribution (GEV) whose cumulative distribution function is

$$\Pr\{\eta(s) \leq z\} = \exp \left[- \left\{ 1 + \xi(s) \frac{z - \mu(s)}{\sigma(s)} \right\}^{-1/\xi(s)} \right], \quad \sigma(s) + \xi(s)(z - \mu(s)) > 0, \quad (1)$$

where $\eta(s)$ denotes the block maxima random variable at location $s \in \mathcal{X}$, and $\mu(s) \in \mathbb{R}$, $\sigma(s) \in (0, \infty)$, $\xi(s) \in \mathbb{R}$ are respectively the location, scale and shape GEV parameters.

For most applications, it is sensible to let the GEV parameters vary over the spatial domain \mathcal{X} so that one must impose a regression structure on these parameters, e.g., $\mu(s) = f_\mu\{\mathbf{x}(s); \boldsymbol{\beta}_\mu\}$ where $\mathbf{x}(s)$

denotes a vector of covariates evaluated at location s . A popular choice is to assume a linear form, e.g., $f_\mu(\mathbf{x}(s); \beta_\mu) = \mathbf{x}^\top(s)\beta_\mu$ but often yields to unrealistically smooth surfaces (Davison et al., 2012). To bypass this hurdle, one can take benefit of using a latent hierarchical model with a conditional independence assumption (Cooley et al., 2007; Casson and Coles, 1999) where the GEV parameters now vary spatially according to some stochastic process, i.e.,

$$\begin{aligned} \eta(s) \mid \{\mu(s), \sigma(s), \xi(s)\} &\stackrel{\text{ind}}{\sim} \text{GEV}\{\mu(s), \sigma(s), \xi(s)\}, & s \in \mathcal{X} \\ \mu(\cdot) &\sim \text{GP}(m_\mu, \gamma_\mu) \\ \sigma(\cdot) &\sim \text{GP}(m_\sigma, \gamma_\sigma) \\ \xi(\cdot) &\sim \text{GP}(m_\xi, \gamma_\xi) \end{aligned} \quad (2)$$

where $\text{GP}(m, \gamma)$ denotes a (univariate) Gaussian process with mean function $m: s \mapsto m(s)$ and covariance function $\gamma: (s_1, s_2) \mapsto \gamma(s_1, s_2)$ and the three Gaussian processes above are usually assumed independent for simplicity.

To the best of our knowledge, statistical developments have focused mainly on the magnitude of extremes, e.g., rainfall amount, while little attention has been paid to some additional features of these events. More precisely, environmental processes are often attached with an angular component, e.g., wind direction. One exception is proposed by Konzen et al. (2021) but the aim was to handle appropriately angular covariates and not any angular outcome. This paper aims at filling this gap by considering a hierarchical Bayesian framework which takes advantage of the conditional independence assumption and is able to handle both extremal and angular features of the data. The paper is organized as follows. Section 2 introduces the projected Gaussian process model. Section 3 gives an extension of model (2) by adding an additional layer corresponding to the projected Gaussian model and details how inference can be done using MCMC techniques. Section 4 gives results of a simulation study while Section 5 applies the proposed methodology to extreme wind speeds in France. The paper ends with a discussion. Specific details on MCMC implementation are deferred to the appendix.

2 The projected Gaussian process model

Parametric statistical models for directional data are often based on three main families: distribution on $[0, 2\pi]$, wrapped distribution on \mathbb{R} and projected distributions (Mardia and Jupp, 2009). This paper focuses on projection methods and more specifically on projected Gaussian distributions as extension to the spatial setting is straightforward. The projected Gaussian model (Gelfand and Wang, 2013) is defined as a random angle θ obtained via the projection of a bivariate Gaussian vector X onto the unit circle $\mathbb{S}^1 = \{x \in \mathbb{R}^2: \|x\|_2 = 1\}$.

Extending the above univariate distribution to the spatial setting amounts to switch the bivariate vector X for a bivariate Gaussian process $\{X(s) = \{X_1(s), X_2(s)\}^\top: s \in \mathcal{X}\}$ with mean function $\mu: s \mapsto \mathbb{E}[X(s)]$ and covariance function $\gamma: (s_1, s_2) \mapsto \Gamma$ where Γ is a 4×4 block-matrix with each block $\Gamma_{i,j} = \text{Cov}\{X(s_i), X(s_j)\}$, $i, j = 1, 2$. The projected Gaussian process (Gelfand and Wang, 2014) is then defined as $\{\theta(s) = \arctan^*\{X_2(s)/X_1(s)\}: s \in \mathcal{X}\}$, and will be denoted as $\theta \sim PG\{\mu, \gamma\}$. Figure 1 plots one realization of the projected Gaussian process and exhibits how it can handle a large variety of behaviours, e.g., multi-modality, asymmetry.

Although no closed form exists for the projected Gaussian process likelihood, inference becomes possible by working within an augmented data framework. More precisely, for some spatial locations $\mathbf{s} = (s_1, \dots, s_k) \in \mathcal{X}^k$, $k \geq 1$, we associate to the angular random vector $\theta(\mathbf{s}) = \{\theta(s_1), \dots, \theta(s_k)\}$ a radial random vector $R(\mathbf{s}) = \{R(s_1), \dots, R(s_k)\}$ so that one can easily switch from polar coordinates $\{R(\mathbf{s}), \theta(\mathbf{s})\}$ to Cartesian ones $X(\mathbf{s}) = R(\mathbf{s})\{\cos \theta(\mathbf{s}), \sin \theta(\mathbf{s})\}^\top$ and where multiplication is done componentwise.

Inference is therefore based on the induced bivariate Gaussian random vector $X(\mathbf{s})$ and it is easily seen

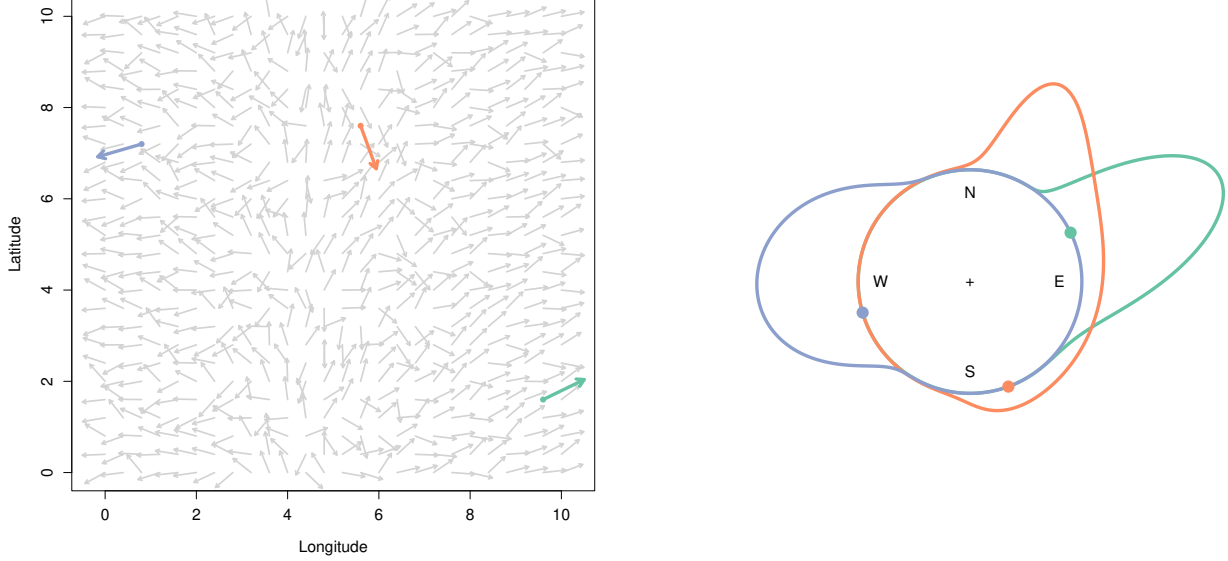


Figure 1: Illustration of the projected Gaussian process. Left: Realization of a projected Gaussian process with three highlighted locations (coloured arrows). Right: projected Gaussian densities at the three highlighted locations. Each blob corresponds to the observed directions

that, for any $\mathbf{r} \in (0, \infty)^k$ and $\mathbf{t} \in [0, 2\pi]^k$, $k \geq 1$, the joint density of the random vector $\{R(\mathbf{s}), \theta(\mathbf{s})\}$ is

$$f_{\mathbf{s}}(\mathbf{r}, \mathbf{t}) = (2\pi)^{-k/2} |\Sigma(\mathbf{s})|^{-1/2} \exp\left(-\frac{\{\mathbf{r}^\top \mathbf{u} - \mu(\mathbf{s})\}^\top \Sigma(\mathbf{s})^{-1} \{\mathbf{r}^\top \mathbf{u} - \mu(\mathbf{s})\}}{2}\right) \prod_{i=1}^k r_i, \quad (3)$$

with

$$\mathbf{u} = \begin{bmatrix} \cos t_1 & \dots & \cos t_k \\ \sin t_1 & \dots & \sin t_k \end{bmatrix}^\top,$$

where $\mu(\mathbf{s})$ and $\Sigma(\mathbf{s})$ are respectively the mean vector and cross-covariance matrix of the Gaussian random vector $X(\mathbf{s})$.

3 Extreme-angular Bayesian hierarchical model

By combining the latent variable for extremes (2) and the projected Gaussian process described in Section 2, one can define what we shall call a spatial extremal-angular Bayesian hierarchical model:

$$\begin{aligned} \theta(\cdot) &| \{m_\theta, \gamma_\theta, \mu(\cdot), \sigma(\cdot), \xi(\cdot)\} \sim \text{PG}(m_\theta, \gamma_\theta), \\ \eta(s) &| \{\mu(s), \sigma(s), \xi(s)\} \stackrel{\text{ind}}{\sim} \text{GEV}\{\mu(s), \sigma(s), \xi(s)\}, \quad s \in \mathcal{X} \\ \mu(\cdot) &| \{m_\mu, \gamma_\mu\} \sim \text{GP}(m_\mu, \gamma_\mu) \\ \sigma(\cdot) &| \{m_\sigma, \gamma_\sigma\} \sim \text{GP}(m_\sigma, \gamma_\sigma) \\ \xi(\cdot) &| \{m_\xi, \gamma_\xi\} \sim \text{GP}(m_\xi, \gamma_\xi) \end{aligned} \quad (4)$$

where prior distributions are put on the mean and covariance function parameters on each (eventually projected) Gaussian processes. The last four lines are identical to Model (2). Further, and as suggested by the conditioning terms, the mean function for the angular process may depend on any relevant spatial covariates such as longitude, latitude or elevation and, more importantly, on GEV parameters. For example,

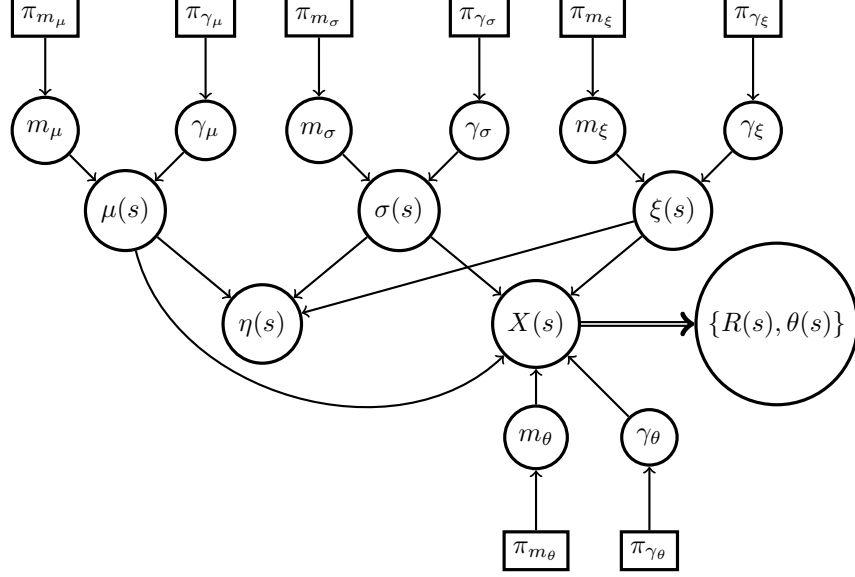


Figure 2: Directed acyclic graph for the extreme–angular hierarchical model with the latent radial process $\{R(s) : s \in \mathcal{X}\}$. A double arrow indicates a deterministic relationship between the two nodes.

a sensible choice may be to use, in addition to geophysical covariates, GEV quantiles to assess whether the angular may be impacted by the extreme values intensities. Figure 2 gives the directed acyclic graph for this model.

Due to the presence of latent processes $m_\mu(\cdot)$, $m_\sigma(\cdot)$, $m_\xi(\cdot)$ and $R(\cdot)$, the likelihood has an integral representation and, working within a Bayesian setting, marginalization across the latent processes is done numerically using MCMC techniques. The Gibbs sampler for Model (4) is similar to that proposed by Cooley et al. (2007) and Gelfand and Wang (2014), but, due to the induced dependence between extremes and angles, some of the full conditional distributions required for a Gibbs sampler are more sophisticated. More precisely, updating the mean function parameters of the Gaussian processes associated to the GEV distributions for locations \mathbf{s} consists in sampling from

$$\pi(m_\mu \mid \dots) \propto \pi\{\mu(\mathbf{s}) \mid m_\mu(\mathbf{s}), \gamma_\mu(\mathbf{s}, \mathbf{s})\} \pi(m_\mu). \quad (5)$$

Note that, Equation 5 corresponds to that of Model 2. Similar expressions are found for the mean function of the GEV scale and shape parameters as well as for the parameters of the covariance functions γ_μ , γ_σ and γ_ξ .

Contrary to Equation 5 the update of the GEV parameters at locations \mathbf{s} differs and now depends on the (augmented) projected Gaussian process. It consists in sampling from

$$\pi\{\mu(s_j) \mid \dots\} \propto \prod_{i=1}^n \pi\{\eta_i(s_j) \mid \mu(s_j), \sigma(s_j), \xi(s_j)\} \pi\{X_i(\mathbf{s}) \mid m_\theta, \gamma_\theta, \mu(\mathbf{s}), \sigma(\mathbf{s}), \xi(\mathbf{s})\} \pi\{\mu(\mathbf{s}) \mid m_\mu, \gamma_\mu\},$$

for $j = 1, \dots, k$ with similar expressions for $\sigma(s_j)$ and $\xi(s_j)$, $j = 1, \dots, k$.

Similarly, and since the radius process $R(\cdot)$ may depend on the GEV parameters, the associated full conditional distributions differ from that given in Gelfand and Wang (2014) and are given by

$$\begin{aligned} \pi\{R_i(\mathbf{s}) \mid \dots\} &\propto \pi\{R_i(\mathbf{s}) \mid \theta_i(\mathbf{s}), m_\theta, \gamma_\theta, \mu(\mathbf{s}), \sigma(\mathbf{s}), \xi(\mathbf{s})\}, \quad i = 1, \dots, n, \\ \pi(m_\theta \mid \dots) &\propto \prod_{i=1}^n \pi\{X_i(\mathbf{s}) \mid m_\theta, \gamma_\theta, \mu(\mathbf{s}), \sigma(\mathbf{s}), \xi(\mathbf{s})\} \pi(m_\theta), \end{aligned}$$

where $\pi(m_\theta | \dots)$ denotes the full conditional distribution of the mean function and $\pi(m_\theta)$ is the associated prior distribution. A similar expression for the cross covariance function γ_θ can be found.

In practice, one usually assume some parametric expressions for the mean and (cross) covariance functions of the latent Gaussian processes and use conjugate prior distributions whenever possible. For instance a sensible choice for the mean function is to assume a Gaussian prior distribution and a linear form for the mean function, i.e., $m_j(\mathbf{s}) = D_j(\mathbf{s})\boldsymbol{\beta}_j$, $j \in \{\mu, \sigma, \xi, \theta\}$, where $D_j(\mathbf{s})$ is the design matrix at location \mathbf{s} .

For the GEV latent processes, a parametric stationary and isotropic covariance function can be used, e.g., a powered exponential covariance $\gamma(s, s+h) = \gamma(\|h\|) = \tau \exp\{- (\|h\|/\lambda)^\kappa\}$. Similarly to get efficient updates for each sill parameters of the Gaussian processes, an inverse Gamma prior distribution may be a relevant choice. Since no conjugate prior distributions exist for the range and the shape parameters λ and κ , a Metropolis–Hastings updating scheme has to be used.

Finally, and to ease inference, it is common practice to assume a stationary isotropic and separable cross covariance function for the bivariate Gaussian process $\{X(s) : s \in \mathcal{X}\}$, i.e.,

$$\gamma_\theta(s, s+h) = \gamma_\theta(\|h\|) = T \otimes \rho(\|h\|), \quad T = \begin{bmatrix} \tau_\theta & \rho_\theta \sqrt{\tau_\theta} \\ \rho_\theta \sqrt{\tau_\theta} & 1 \end{bmatrix}, \quad \tau_\theta > 0, \quad \rho_\theta \in (-1, 1),$$

where \otimes denotes the Kronecker product, ρ is any parametric correlation function, e.g., powered exponential, $\tau_\theta = \text{Var}\{R(s) \cos \theta(s)\}$ and ρ_θ is the cross-correlation, i.e., $\rho_\theta(s) = \text{Cor}\{R(s) \cos \theta(s), R(s) \sin \theta(s)\}$, $s \in \mathcal{X}$. As suggested by Gelfand and Wang (2013), we set $\text{Var}\{R(s) \sin \theta(s)\} = 1$ to ensure identifiability of the parameters. Explicit expressions for these full conditional distributions are postponed to the Appendix.

Algorithm 1: Pointwise predictive posterior predictions from the extreme–angular model.

input : A Markov chain $\{\psi_t : t = 1, \dots, N\}$ sampled from the Gibbs sampler introduced above and a new location $s_* \in \mathcal{X}$.

output: Predictive posterior predictions of an unknown quantity $U(s_*)$.

- 1 **for** $t = 1, \dots, N$ **do**
 - /* Conditional sampling of the GEV parameters */
 - 2 Sample $\mu_t(s_*)$ from the conditional distribution $\mu(s_*) | \mu(\mathbf{s}), \psi_t$;
 - 3 Sample $\sigma_t(s_*)$ and $\xi_t(s_*)$ in the same way;
 - /* Conditional sampling for the angular component */
 - 4 Sample $\theta_t(s_*)$ from the conditional distribution $\theta(s_*) | \mu(\mathbf{s}), \sigma(\mathbf{s}), \xi(\mathbf{s}), \psi_t$;
- 5 **end**
- 6 Return the $U(s_*)$ -estimator $\hat{U}(\psi_1(s_*), \dots, \psi_N(s_*))$;

Spatial models often aim at doing predictions at unobserved locations $s_* \in \mathcal{X}$ such as the values of the GEV parameters, return levels or the circular mode of the posterior distribution of $\theta(s_*)$. Within a Bayesian framework, it is typically done through the posterior predictive distribution

$$\int \pi(\eta(s_*), \theta(s_*) | \boldsymbol{\psi}, \mathcal{D}_n) \pi(\boldsymbol{\psi} | \mathcal{D}_n) d\boldsymbol{\psi},$$

where $\mathcal{D}_n = \{(\eta_i(s_j), \theta_i(s_j)) : i = 1, \dots, n, j = 1, \dots, k\}$ and $\boldsymbol{\psi}$ is the parameter vector of the model. As expected, the above integral representation has no closed form and, similarly to the Gibbs sampler introduced above, one has to resort to numerical integration where each state of the generated Markov chain is browsed, see Algorithm 1. Further, when the unknown quantity $U(s_*)$ has no closed form, one might use an empirical version of $U(s_*)$ such as empirical quantiles of order p to get a sensible estimator.

4 Simulation study

In order to assess the performance of our algorithm, we run a simulation study with three different dependence settings as shown in Table 1 and varying sample sizes n and number of locations k . In Configuration I, the

Table 1: Configuration settings for the simulation study. The angular mean function is set to $m_\theta(s) = \{m_{\theta,1}(s), m_{\theta,2}(s)\}^\top$. For each configuration the latent GEV parameter processes (μ, σ, ξ) were held fixed respectively to Gaussian processes with mean functions $m_\mu(s) = 2 - 3\text{lon}(s) - 2\text{lat}(s)$, $m_\sigma(s) = 2 + \text{lat}(s)$, $m_\xi = 0.05$, sill parameters 0.1, 0.5, 0.05 and range parameters 1, 2, 3 respectively.

	σ^2	ρ	$m_{\theta,1}(s)$	$m_{\theta,2}(s)$	Modality
I: Independent	0.4	0.3	0.5	0	Multimodal
II: Light	0.4	0.3	0.5	$2\xi(s)$	Multimodal
III: Strong	1.0	0	$10 + 0.5\mu(s)$	0	Unimodal

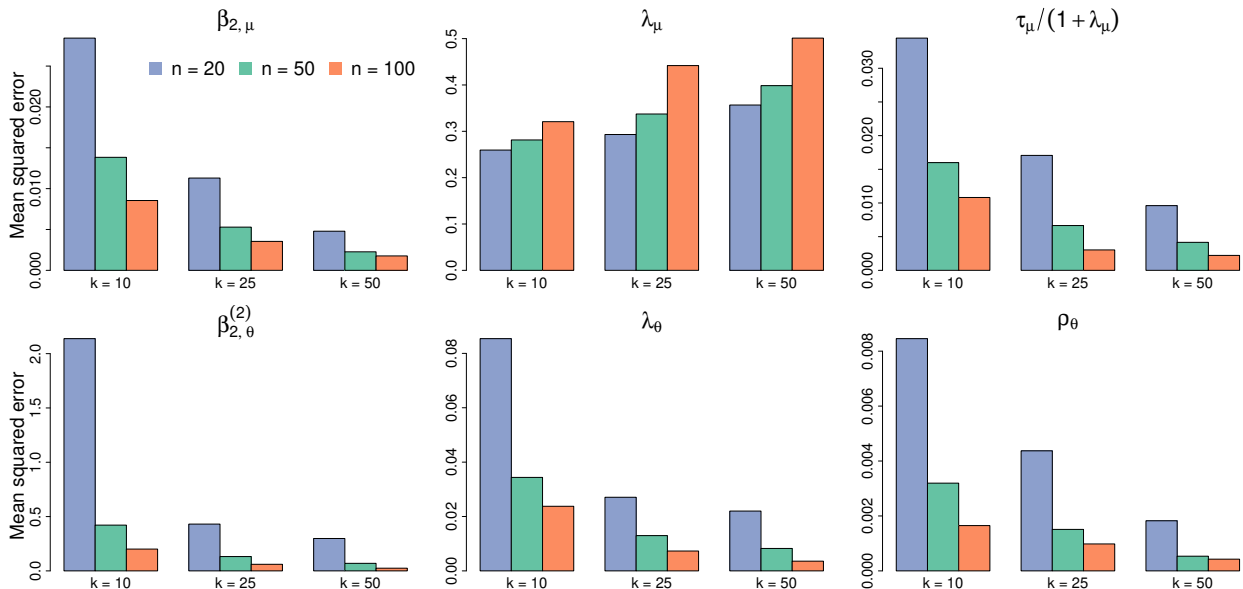


Figure 3: Evolution of the mean squared error (MSE) of parameters with varying number of observations n and locations k for Configuration II. Top: MSE for the regression (left), range (middle) parameters and quotient of scale and range (right) of the covariance function of the Gaussian process μ . Bottom: MSE for regression parameter (left), range parameter (middle) and correlation parameter (right) of the projected Gaussian process θ .

angular mean function m_θ is independent of the GEV parameters and, consequently, angles and extremes are assumed to be independent. With this setting, Algorithm 1 is equivalent to the use of two independent samplers: one for the GEV component and one for the angular component. Configuration II provides a linear dependence between angles and extremes through the shape parameter of the GEV. However, since the Gaussian process for the shape parameter has constant mean and low variance, the shape parameter is roughly constant over \mathcal{X} and, as so, dependence between angles and extremes magnitudes is limited. On the contrary, in Configuration III the angular mean function depends on the GEV location parameter which varies significantly over \mathcal{X} yielding to a strong dependence between angles and extremes magnitudes.

Working within a fixed domain framework, i.e., the spatial domain \mathcal{X} is fixed, we numerically analyse infill and sample size asymptotics, i.e., where k tends to infinity n being fixed and conversely. For each dependence setting of Table 1, we consider the cases where $k = 10, 25, 50$ and $n = 20, 50, 100$, leading to 27 configurations overall.

Figure 3 shows the evolution of the mean squared error as the number of locations k and replicates n vary for a selected panel of parameters. The top row of Figure 3 focuses on the Gaussian process of the GEV location parameter. More precisely, results are shown for $\beta_{2,\mu}$, a regression parameter of the mean function

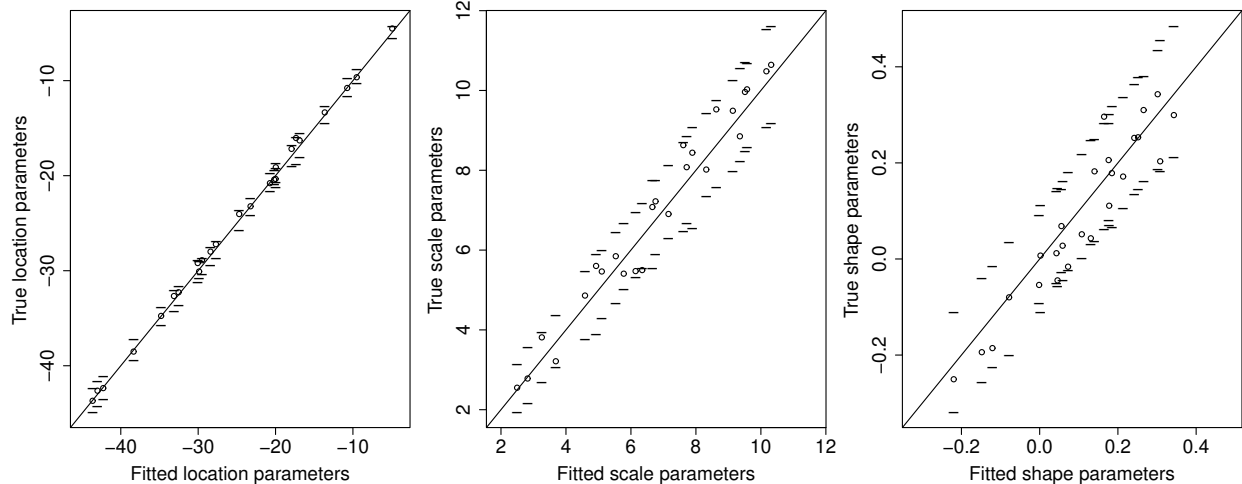


Figure 4: Posterior median (with 95% credible intervals) for the GEV parameters at $k = 25$ locations and with $n = 50$ observations for Configuration II.

m_μ , the range parameter λ_μ of the covariance function γ_μ as well as the ratio $\tau_\mu/(1 + \lambda_\mu)$ where τ_μ is the sill parameter of γ_μ . As expected, the mean squared error for $\beta_{2,\mu}$ decreases as both k and n increase. Indeed, as k increases, the number of GEV parameters increases and the linear structure $\mathbb{E}[\mu(s)] = x(s)^\top \beta_\mu$ becomes more apparent. Similarly, as the number of replicates n increases, the GEV parameters estimates become increasingly more accurate and the above linear structure has less noise. Results for other parameters and dependence configurations show similar patterns.

Interestingly, the mean squared error for λ_μ has a completely different behaviour and no convergence is visible. A similar pattern is seen for the sill parameter τ_μ . As shown in Zhang (2004), there is no consistency in the estimation of both the sill and range parameters of a Gaussian process with a single realization. This result applies to our model as each location has a single set of GEV parameters and, consequently, a single realization of the Gaussian processes.

The bottom row of Figure 3 is similar to the top row with an emphasis on the angular component, namely $\beta_{2,\theta}^{(2)}$, ρ_θ and λ_θ . As expected and using the same arguments as the ones stated previously, the evolution of the mean squared error $\beta_{2,\theta}^{(2)}$ is similar to that for $\beta_{2,\mu}$. There is however a subtle difference in the estimation of the parameters of the bivariate Gaussian process $\{\mathbf{X}(s) : s \in \mathcal{X}\}$ compared to that for the GEV parameters, e.g., $\{\mu(s) : s \in \mathcal{X}\}$. Contrary to the latter case, parameters are now estimated from $n > 1$ independent replicates and no consistency issues exist.

At first sight, the above lack of consistency may cause problems in the estimation of the GEV parameters or related quantities such as quantiles. Fortunately, Zhang (2004) have shown that the ratio of the sill and range parameters can be consistently estimated (see top right panel of Figure 3) and, more importantly, that there is no impact on the predictions of the GEV parameters. Figure 4 compares the true GEV parameters from that estimated from our approach. As expected, one can see that the predicted GEV parameters match the theoretical ones. The shape parameter being usually harder to estimate, slightly worse performances can be seen.

We now assess the predictive performance of the proposed model and, more specifically, that associated to the prediction of some angular quantity over the spatial domain \mathcal{X} . As the projected Gaussian process may be multimodal, some care is needed in defining the quantity of interest and, in the sequel, we will focus on the (main) posterior mode for the angle. Figure 5 shows prediction maps for Configuration II. With this setting, the predictive posterior distribution is bimodal and may introduce spatial discontinuities in the posterior modes. To be more specific, there is a cutoff value for the shape parameter for which if exceeded, the modal direction is top-right and bottom-right otherwise. The left panel of Figure 5 illustrates the relationship

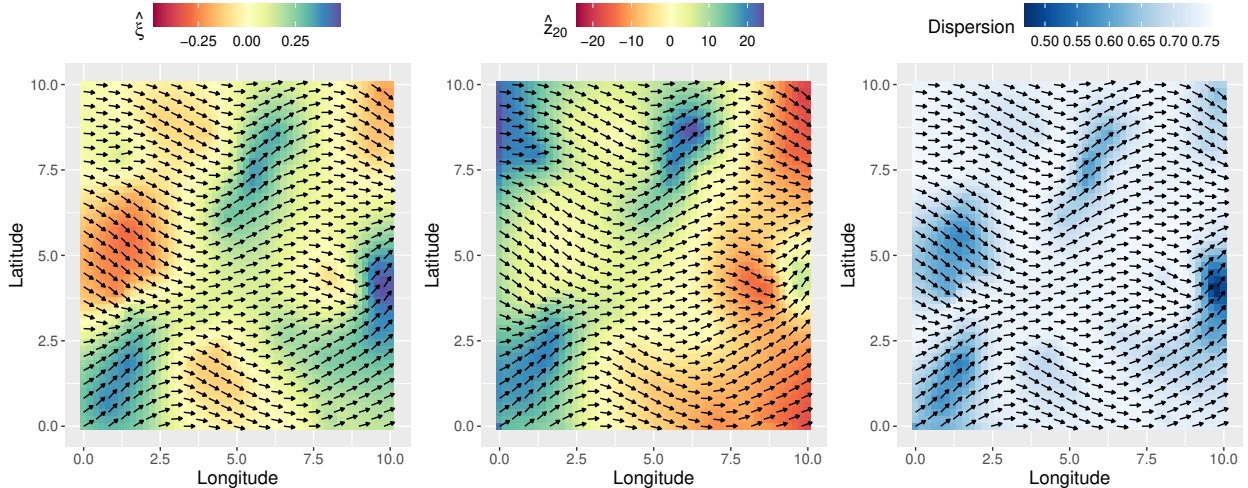


Figure 5: Prediction maps for Configuration II with $n = 100$ observations and $k = 50$ locations. All predictions are derived from the predictive posterior distribution. Left: Prediction of the main direction and GEV shape parameter. Middle: Prediction of the main direction and GEV quantiles of order 0.95. Right: prediction of the main direction and circular standard deviation.

between predicted angles and shape parameters as well as the aforementioned cutoff behaviour. The middle panel is similar to the previous one except that predicted quantiles of order 0.95 are now overlaid. Since GEV quantiles are function of the GEV location, scale and shape parameters, overall, the same behaviour can be seen. However, due to the analytic expression for GEV quantiles, there is no cut-off behaviour as the one stated previously. For instance, quantiles in the outermost South-East sub-region are lower due to the contribution of the location parameter as opposed to the general behaviour “South-East direction for small return levels”. The right panel shows the relationship between predicted angles and the angular dispersion. One can see that the two modes have different impact. More precisely, one can see that the mode associated to the North-East direction is the preponderant one and has large dispersion whereas that associated to the South-East direction only dominates after a rare cut-off exceedance and has less dispersion.

5 Application

The data, freely available from Météo-France, consist in annual maxima of wind speeds and their associated wind direction observed at a height of 10m for $k = 110$ weather stations in France and recorded from 1994 to 2023. Figure 6 plots the spatial distribution of the weather stations, the annual maxima wind speed time series and the empirical distributions of wind directions associated to the annual maxima for two selected stations. One can see that annual wind speed maxima at Calais are larger than in Aix-en-Provence and appear to have a single main direction (South-West) while extreme wind speeds at Aix-en-Provence may originate from two different directions (North-North-West and South-East). As expected, the spatial distribution of extreme wind speeds is not stationary over France; neither is that for wind directions. Modelling such non-stationary behaviour is challenging, but it is hoped that thanks to its flexibility, the use of Model (4) will be able to cope with those two different types of non-stationarity.

To perform model selection for Bayesian hierarchical models, a useful performance metric is the Widely Applicable Information Criterion (WAIC) (Watanabe, 2013) whose focus is on predictive performances. In the same vein as the Akaike Information Criterion, WAIC penalizes model complexity but is more relevant for performing model selection in a setting. Table 2 displays performance scores for a bunch of competitive models with a varying degree of complexity. Note that in addition to geophysical covariates such as longitude, latitude and elevation, some models may also consider extreme wind speed quantiles for the modelling of

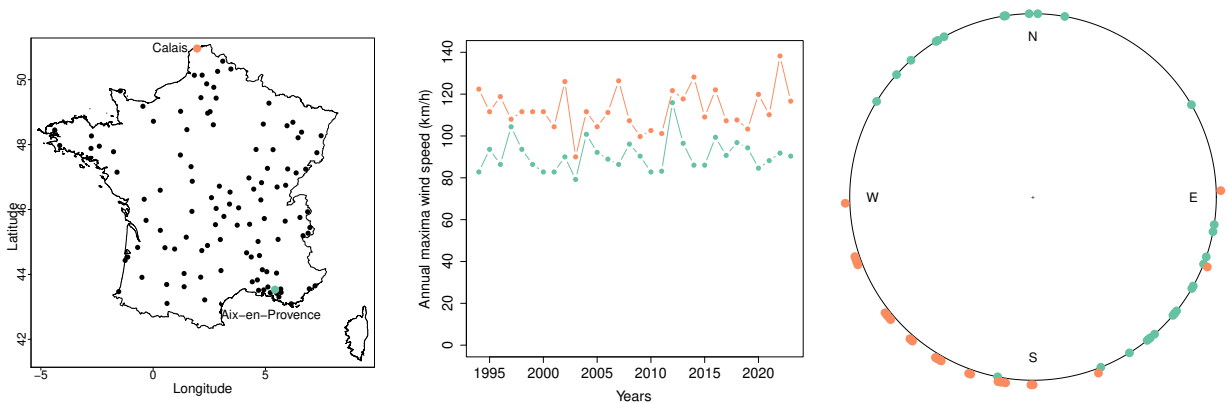


Figure 6: Wind data in continental France. From left to right: study region and locations of the weather stations; times series of annual maxima wind speed and empirical distribution of angles (direction of extreme wind) at two selected stations: Calais (orange) and Aix-en-Provence (green).

Table 2: Widely Applicable Information Criterion (WAIC) for selected models. All models have $m_\xi(s) = \beta_0$. The function q is the quantile function of the GEV distribution.

		WAIC $_\theta$	WAIC $_\eta$	WAIC
Model 0		14,702	16,343	31,045
	$m_\mu(s) = \beta_0 + \beta_1 \text{alt}(s)$			
	$m_\sigma(s) = \beta_0 + \beta_1 \text{lon}(s) + \beta_2 \text{lat}(s) + \beta_3 \text{alt}(s)$			
	$m_{\theta,1}(s) = \beta_0 + \beta_1 \text{lon}(s) + \beta_2 \text{lat}(s) + \beta_3 \text{alt}(s)$			
	$m_{\theta,2}(s) = \beta_0 + \beta_1 \text{lon}(s) + \beta_2 \text{lat}(s) + \beta_3 \text{alt}(s)$			
Model 1	Model 0 with	14,096	16,581	30,677
	$m_{\theta,1}(s) = \beta_0 + \beta_1 \text{lon}(s) + \beta_2 \text{lat}(s) + \beta_3 \text{alt}(s) + \beta_4 \mu(s) + \beta_5 \sigma(s)$			
	$m_{\theta,2}(s) = \beta_0 + \beta_1 \text{lon}(s) + \beta_2 \text{lat}(s) + \beta_3 \text{alt}(s) + \beta_4 \mu(s) + \beta_5 q(0.95 \mu, \sigma, \xi)$			
Model 2	Model 0 with	13,823	16,412	30,235
	$m_{\theta,1}(s) = \beta_0 + \beta_1 \text{lon}(s) + \beta_2 \text{lat}(s) + \beta_3 \text{alt}(s) + \beta_4 q(0.95 \mu, \sigma, \xi) + \beta_5 q(0.99 \mu, \sigma, \xi)$			
Model 3	Model 2 with	13,800	16,352	30,152
	$m_{\theta,1}(s) = \beta_0 + \beta_1 q(0.95 \mu, \sigma, \xi) + \beta_2 q(0.99 \mu, \sigma, \xi)$			
Model 4	Model 2 with	13,822	16,364	30,186
	$m_\mu(s) = \beta_0$			
	$m_\sigma(s) = \beta_0 + \beta_1 \text{lat}(s) + \beta_2 \text{alt}(s)$			
Model 5	Model 3 with	13,858	16,418	30,276
	$m_\mu(s) = \beta_0$			
	$m_\sigma(s) = \beta_0 + \beta_1 \text{lat}(s) + \beta_2 \text{alt}(s)$			

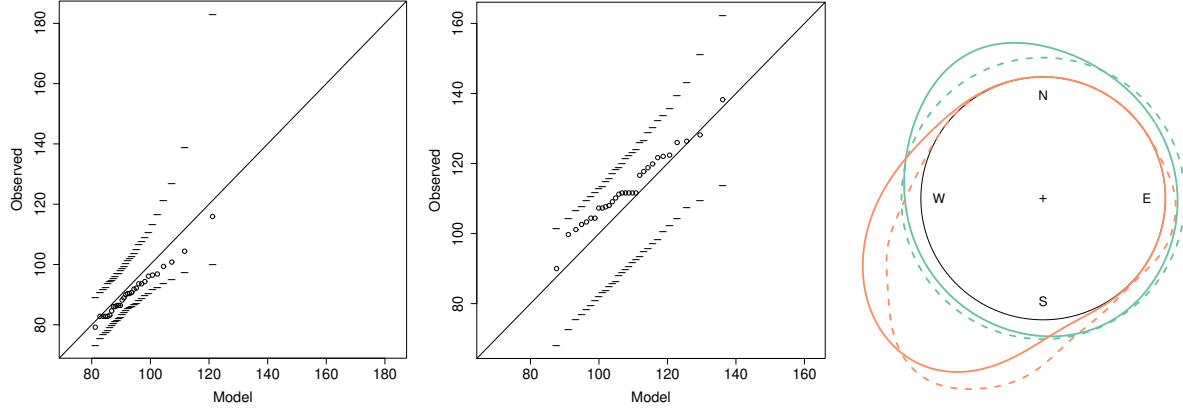


Figure 7: Model checking. The left and middle panels compare the observed and predicted maxima for the Aix-en-Provence and Calais stations (with 95% confidence envelopes). The right panel compares the predicted angular distributions (solid lines) and the angular kernel density estimates (dashed lines).

Table 3: Posterior median and 95% credible intervals (in parenthesis) for Model 3.

Generalized extreme value layer							
	β_0	β_{lon}	β_{lat}	β_{alt}	τ	λ	
μ	95(93,97)	—	—	2.4(-2.4,7.3)	78(60,102)	8(1,20)	
σ	2(-13,18)	-0.3(-0.7,0.1)	0.19(-0.15,0.53)	2.9(1.2,4.9)	6.5(4,11)	104(57,184)	
ξ	-0.07(-0.1,0)	—	—	—	0.01(0.00,0.01)	127(75,225)	
Angular layer							
	β_0	$\beta_{q(0.95)}$	$\beta_{q(0.99)}$		τ	λ	ρ_θ
$m_{\theta,1}$	-1.7(-3,-0.4)	-0.20(-0.26,-0.15)	0.18(0.14,0.23)				
$m_{\theta,2}$	8.4(7.1,9.7)	0.03(0.01,0.05)	-0.19(-0.22,-0.16)	β_{alt}	0.6(0.5,0.7)	45(41,49)	-0.3(-0.4,-0.2)

wind speed direction. The rationale for this type of dependence is that it may be sensible to assert that the largest extreme wind speeds are attached to a very specific wind direction.

Although a large number of models have been considered, and to save space, results are only presented for a limited number of configurations. Model 0 assumes independence between the extreme value process $\{\eta(s) : s \in \mathcal{X}\}$ and the angular process $\{\theta(s) : s \in \mathcal{X}\}$ while all the other models assume dependence. One can see that the independent model performs best in predicting extreme wind speeds but is poor in predicting wind direction. Hence, for this application, it seems that the knowledge of wind direction is irrelevant in modelling wind speeds. Model 3 appears to be the most accurate as it is almost as efficient as the independent model in predicting wind speed and has good predictive performances for wind directions. This model makes use of the 20 and 100–years return levels and may indicate that the original assumption that the largest extreme wind speeds impact wind directions is sensible.

Figure 7 assesses the performance of Model 3. The left panel compares predicted observations and that observed wind speeds for the two highlighted stations of Figures 6. Although predictions show some bias, predictions are rather good. Better performances are likely to be obtained by using additional geophysical covariates, but unfortunately, such additional covariates were not provided in the data set who was limited to longitude, latitude and altitude only. The right panel compares the observed directions and the fitted angular densities for these two locations. Predictions appear to be accurate and one can see that our model is able to cope with both unimodal (Calais) and bi-modal (Aix-en-Provence) distributions. Similar results were obtained for all the other stations.

Table 3 shows parameter estimates for Model 3. Interestingly, the sum between the parameter estimates associated to the 20 and 100–years return levels varies around 0, i.e., $\beta_{q(0.95)} + \beta_{q(0.99)} \approx 0$. As $q(p_1) - q(p_2) = \sigma c(p_1, p_2, \xi)$ where $q(p)$ is the quantile function of a GEV(μ, σ, ξ) and $c(p_1, p_2, \xi)$ only depends on p_1, p_2 and

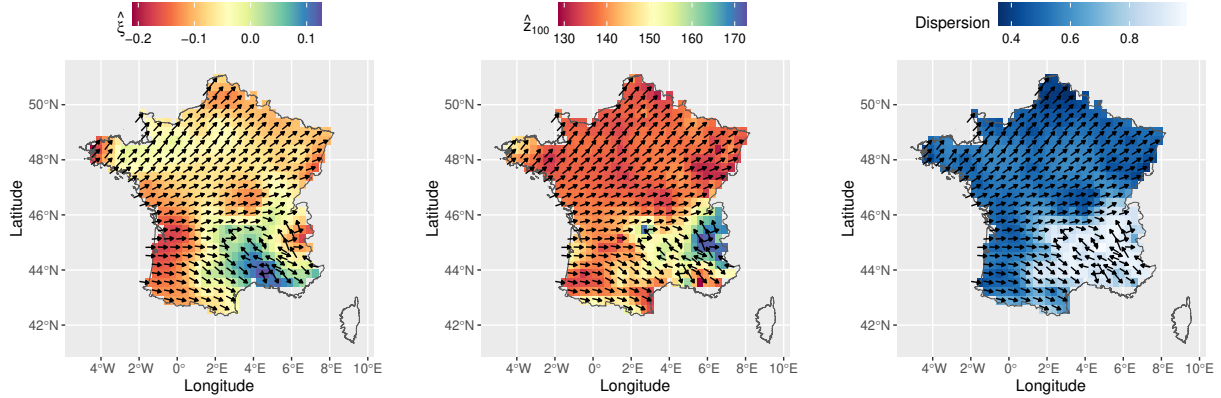


Figure 8: Pointwise prediction maps of the wind direction and the GEV shape parameter (left), 100-year return level (middle) and the wind direction dispersion (right).

ξ , extreme wind speed direction appear to depend on the spread, skewness and higher order moments of extreme wind speeds but not their central tendency.

Figure 8 gives predictions maps from Model 3. One can see that the shape parameter appears to be rather constant over France apart from the Atlantic coastline and the South-East part of France. Similarly, the 100-years return levels are larger in the most Western part, more precisely in the western part of Brittany and Landes as well as the South-East part of France—especially in the French Alps. Overall, the wind direction dispersion is rather limited. One exception is the South-East part of France where the angular dispersion is much larger indicating that wind speed directions may vary roughly over space in that region. Further, as expected, one can see that extreme wind event appears to come from West but tends to change smoothly to the South West direction for the Northern part of France. Again the South-East part of France and the Alps show a completely different behaviour. For the former, extreme wind events appear to come from West-North and is in agreement with the observational study of Obermann et al. (2018). The behaviour in the French Alps is more erratic which may be explained that the wind trajectory has to follow the valley in mountainous regions.

Conclusion

Since many environmental processes are associated with an angular component, this paper proposed a Bayesian hierarchical model to handle such features by allowing the joint modelling of extremes and angular components. An inferential framework has been proposed whose performances were assessed through a simulation study. A lack of consistency for some Gaussian processes dependence parameters has been illustrated but, fortunately, did not impact prediction of relevant quantities of interest such as return levels. An application to extreme wind speeds and direction in continental France was conducted. Results show that extreme wind speeds in the Atlantic part of France is mainly dominated by West directions. A different behaviour is seen for the Mediterranean part of France where extreme winds arise from multiple winds patterns, i.e., north and south directions. This leads to a multimodal angular distribution, whose low-scale spatial variations are harder to recover with a general model.

Although this paper illustrates the usefulness of the proposed model, it has some limitations. First, the model is time stationary and cannot handle situations where there is a clear impact of climate change. An extension to the non-stationary case may be considered using a non-stationary covariance structure or time dependent model parameters. Second, as a consequence of the conditional independence assumption, areal quantities such as total amount of rainfall in a sub-domain is not possible. To overcome this problem, the conditional independence assumption should be relaxed and, in accordance to the extreme value theory, a

max-stable should now be considered. The use max-stable process is however challenging since the likelihood associated to these processes is extremely CPU demanding and one has to develop an elegant framework to overcome this computational burden.

Appendix: Gibbs sampler

Inference for our latent extreme-angular Bayesian hierarchical model may be performed using a Gibbs sampler, whose steps we now describe. To ease notations, we define $\mathbf{R}_t = \{R_t(s_1), \dots, R_t(s_k)\}$ and $\boldsymbol{\mu}_t = \{\mu_t(s_1), \dots, \mu_t(s_k)\}$ with similar for the GEV scale and shape parameters. Given a current value of the Markov chain

$$\psi_t = (\mathbf{R}_t, \boldsymbol{\mu}_t, \boldsymbol{\sigma}_t, \boldsymbol{\xi}_t, \rho_t, \tau_\mu, \tau_{\theta,t}, \tau_{\sigma,t}, \tau_{\xi,t}, \lambda_{\theta,t}, \lambda_{\mu,t}, \lambda_{\sigma,t}, \lambda_{\xi,t}, \boldsymbol{\beta}_{\theta,t}, \boldsymbol{\beta}_{\mu,t}, \boldsymbol{\beta}_{\sigma,t}, \boldsymbol{\beta}_{\xi,t}),$$

the next state ψ_{t+1} of the chain is obtained as follows.

Step 1: Updating the GEV parameters at each site

Each component of $\boldsymbol{\mu} = \{\mu(s_1), \dots, \mu(s_k)\}$ is updated singly according to the following scheme. Generate a proposal $\mu_p(\mathbf{s})$ from a symmetric random walk and compute the acceptance probability

$$\alpha\{\mu(\mathbf{s}), \mu_p(\mathbf{s})\} = \min\{1, r_1\{\mu(\mathbf{s}), \mu_p(\mathbf{s})\}r_2\{\mu(\mathbf{s}), \mu_p(\mathbf{s})\}r_3\{\mu(\mathbf{s}), \mu_p(\mathbf{s})\}\},$$

with

$$\begin{aligned} r_1\{\mu(\mathbf{s}), \mu_p(\mathbf{s})\} &= \prod_{j=1}^k \frac{\pi\{\eta(s_j) \mid \mu_p(s_j), \sigma(s_j), \xi(s_j)\}}{\pi\{\eta(s_j) \mid \mu(s_j), \sigma(s_j), \xi(s_j)\}} \\ r_2\{\mu(\mathbf{s}), \mu_p(\mathbf{s})\} &= \prod_{i=1}^n \frac{\pi\{R_i(\mathbf{s}), \theta_i(\mathbf{s}) \mid \mu_p(\mathbf{s}), \sigma(\mathbf{s}), \xi(\mathbf{s}), \boldsymbol{\beta}_\theta, \rho, \tau_{\theta,t}\}}{\pi\{R_i(\mathbf{s}), \theta_i(\mathbf{s}) \mid \mu(\mathbf{s}), \sigma(\mathbf{s}), \xi(\mathbf{s}), \boldsymbol{\beta}_\theta, \rho, \tau_{\theta,t}\}} \\ r_3\{\mu(\mathbf{s}), \mu_p(\mathbf{s})\} &= \frac{\pi(\boldsymbol{\mu}_p \mid \boldsymbol{\beta}_\mu, \tau_\mu, \lambda_\mu)}{\pi(\boldsymbol{\mu} \mid \boldsymbol{\beta}_\mu, \tau_\mu, \lambda_\mu)} \end{aligned}$$

where r_1 is a ratio of GEV likelihoods, r_2 a ratio of projected Gaussian likelihoods and r_3 a ratio of multivariate Gaussian likelihoods. With probability $\alpha\{\mu(\mathbf{s}), \mu_p(\mathbf{s})\}$, the $\mu(\mathbf{s})$ component of ψ_{t+1} is set to $\mu_p(\mathbf{s})$; otherwise it remains at $\mu(\mathbf{s})$. The scale and shape parameters are updated similarly.

Due to possible components related to μ, σ or ξ , the design matrix D_θ (related to the regression parameter $\boldsymbol{\beta}_\theta$) needs to be updated each time one of those parameters is changed.

Step 2: Updating the radius at each site and replicate

Components of $\mathbf{R}_i = \{R_i(s_1), \dots, R_i(s_k)\}$, $i = 1, \dots, n$, are updated one by one according to the following scheme. Generate a proposal $R_{p,i}(s_j)$ from a log-normal distribution and accept with probability

$$\alpha\{R_i(s_j), R_{p,i}(s_j)\} = \min\left\{1, \frac{\pi(\mathbf{R}_{p,i}, \boldsymbol{\theta}_i \mid \boldsymbol{\mu}, \boldsymbol{\sigma}, \boldsymbol{\xi}, \boldsymbol{\beta}_\theta, \tau_{\theta,t}, \rho, \lambda_\theta)}{\pi(\mathbf{R}_i, \boldsymbol{\theta}_i \mid \boldsymbol{\mu}, \boldsymbol{\sigma}, \boldsymbol{\xi}, \boldsymbol{\beta}_\theta, \tau_{\theta,t}, \rho, \lambda_\theta)}\right\},$$

i.e., a ratio of radial Gaussian likelihoods, based on (3).

Step 3: Updating the angle regression parameters

Due to the use of conjugate priors, $\boldsymbol{\beta}_\theta$ is drawn directly from a multivariate Gaussian distribution having covariance matrix and mean vector

$$\{(\Sigma_\theta^*)^{-1} + nD_\theta^T \Sigma_\theta^{-1} D_\theta\}^{-1}, \quad \{(\Sigma_\theta^*)^{-1} + D_\theta^T \Sigma_\theta^{-1} D_\theta\}^{-1} \left\{ (\Sigma_\theta^*)^{-1} \boldsymbol{\mu}_\theta^* + D_\theta^T \Sigma_\theta^{-1} \sum_{i=1}^n \mathbf{X}_i \right\}$$

where $\boldsymbol{\mu}_\theta^*$ and Σ_θ^* are the mean vector and covariance matrix of the prior distribution for $\boldsymbol{\beta}_\mu$, D_θ is the design matrix related to the regression coefficients $\boldsymbol{\beta}_\theta$, \mathbf{X}_i is the vector $(\mathbf{R}_i \cos(\boldsymbol{\theta}_i) \quad \mathbf{R}_i \sin(\boldsymbol{\theta}_i))^\top$ and Σ_θ the covariance matrix of \mathbf{X}_i .

Step 4: Updating the GEV regression parameters

Due to the use of conjugate priors, β_μ is drawn directly from a multivariate Gaussian distribution having covariance matrix and mean vector

$$\{(\Sigma_\mu^*)^{-1} + D_\mu^T \Sigma_\mu^{-1} D_\mu\}^{-1}, \quad \{(\Sigma_\mu^*)^{-1} + D_\mu^T \Sigma_\mu^{-1} D_\mu\}^{-1} \{(\Sigma_\mu^*)^{-1} \mu_\mu^* + D_\mu^T \Sigma_\mu^{-1} \mu\}$$

where μ_μ^* and Σ_μ^* are the mean vector and covariance matrix of the prior distribution for β_μ , D_μ is the design matrix related to the regression coefficients β_μ and Σ_μ the covariance matrix of μ . Again the regression parameters for the GEV scale and shape parameters are updated similarly.

Step 5: Updating the sill parameters of the covariance function

τ_μ is drawn directly from an inverse Gamma distribution whose shape and rate parameters are

$$\frac{k}{2} + \kappa_{\tau_\mu}^*, \quad \theta_{\tau_\mu}^* + \frac{1}{2} \tau_\mu (\mu - D_\mu \beta_\mu)^T \Sigma_\mu^{-1} (\mu - D_\mu \beta_\mu),$$

where $\kappa_{\tau_\mu}^*$ and $\theta_{\tau_\mu}^*$ are respectively the shape and scale parameters of the inverse Gamma prior distribution. The sill parameters of the covariance function for the GEV scale and shape parameters are updated similarly.

Step 6: Updating the projected Gaussian parameters

To update the parameter τ_θ , we generate a proposal $\tau_{\theta,p}$ from a log-normal distribution and compute the acceptance probability

$$\alpha\{\tau_\theta, \tau_{\theta,p}\} = \min \left\{ 1, \frac{\pi(\mathbf{R}, \boldsymbol{\theta} \mid \boldsymbol{\mu}, \boldsymbol{\sigma}, \boldsymbol{\xi}, \boldsymbol{\beta}_\theta, \tau_{\theta,p}, \rho, \lambda_\theta) \pi(\tau_{\theta,p} \mid \kappa_{\tau_\theta}^*, \theta_{\lambda_\theta}^*)}{\pi(\mathbf{R}, \boldsymbol{\theta} \mid \boldsymbol{\mu}, \boldsymbol{\sigma}, \boldsymbol{\xi}, \boldsymbol{\beta}_\theta, \tau_{\theta,t}, \rho, \lambda_\theta) \pi(\tau_{\theta,t} \mid \kappa_{\tau_\theta}^*, \theta_{\lambda_\theta}^*)} \frac{\tau_{\theta,p}}{\tau_\theta} \right\},$$

a ratio of projected Gaussian likelihood times the ratio of the prior densities with a correction due to the use of non symmetric proposal distribution and where $\kappa_{\tau_\theta}^*$ and $\theta_{\lambda_\theta}^*$ are respectively the shape and scale parameters of the Gamma prior distribution. With probability $\alpha\{\tau_\theta, \tau_{\theta,p}\}$, the τ_θ component of $\boldsymbol{\psi}_{t+1}$ is set to $\tau_{\theta,p}$; otherwise it remains at $\tau_{\theta,t}$. The parameter λ is updated similarly as well as the parameter ρ except that, for the latter parameter, we use the following symmetric proposal distribution $\rho_p \sim \rho + U(-\epsilon_\rho, \epsilon_\rho)$ and consequently no correction like ρ_p/ρ is required.

Step 7: Updating the range parameters of the covariance function

To update the parameter λ_μ , we generate a proposal $\lambda_{\mu,p}$ from a log-normal distribution and compute the acceptance probability

$$\alpha(\lambda_\mu, \lambda_{\mu,p}) = \min \left\{ 1, \frac{\pi(\boldsymbol{\mu} \mid \tau_\mu, \lambda_{\mu,p}, \boldsymbol{\beta}_\mu)}{\pi(\boldsymbol{\mu} \mid \tau_\mu, \lambda_\mu, \boldsymbol{\beta}_\mu)} \left(\frac{\lambda_{\mu,p}}{\lambda_\mu} \right)^{\kappa_{\lambda_\mu}^* - 1} \exp \left(\frac{\lambda_\mu - \lambda_{\mu,p}}{\theta_{\lambda_\mu}^*} \right) \frac{\lambda_{\mu,p}}{\lambda_\mu} \right\},$$

a ratio of multivariate Normal densities times the ratio of the prior densities and that of the proposal densities and where $\kappa_{\lambda_\mu}^*$ and $\theta_{\lambda_\mu}^*$ are respectively the shape and the scale parameters of the Gamma prior distribution. With probability $\alpha(\lambda_\mu, \lambda_{\mu,p})$, the λ_μ component of $\boldsymbol{\psi}_{t+1}$ is set to $\lambda_{\mu,p}$; otherwise it remains at λ_μ . The range parameters related to the scale and shape GEV parameters are updated similarly. If the covariance family has a shape parameter like the powered exponential or the Whittle–Matérn covariance functions, this is updated in the same way.

References

- Casson, E. and Coles, S. (1999). Spatial regression models for extremes. *Extremes*, 1(4):449–468.
- Cooley, D., Nychka, D., and Naveau, P. (2007). Bayesian spatial modeling of extreme precipitation return levels. *Journal of the American Statistical Association*, 102(479):824–840.

- Davison, A., Padoan, S., and Ribatet, M. (2012). Statistical modelling of spatial extremes. Statistical Science, 7(2):161–186.
- Dombry, C., Engelke, S., and Oesting, M. (2017). Bayesian inference for multivariate extreme value distributions. Electronic Journal of Statistics, 11(2):4813 – 4844.
- Gelfand, A. and Wang, A. (2013). Directional data analysis under the general projected normal distribution. Statistical Methodology, pages 113–127.
- Gelfand, A. and Wang, A. (2014). Modeling space and space-time directional data using projected gaussian processes. Journal of the American Statistical Association.
- Huser, R., Dombry, C., Ribatet, M., and Genton, M. (2019). Full-likelihood inference for max-stable processes. Stat, 8(1):e218.
- Konzen, E., Neves, C., and Jonathan, P. (2021). Modeling nonstationary extremes of storm severity: Comparing parametric and semiparametric inference. Environmetrics, 32(4):e2667.
- Mardia, K. and Jupp, P. (2009). Directional statistics. John Wiley and Sons, Hoboken, New Jersey.
- Obermann, A., Bastin, S., Belamari, S., Conte, D., Gaertner, M. A., Li, L., and Ahrens, B. (2018). Mistral and tramontane wind speed and wind direction patterns in regional climate simulations. Climate Dynamics, 51.
- Watanabe, S. (2013). A widely applicable bayesian information criterion. Journal of Machine Learning Research, 14(27):867–897.
- Zhang, H. (2004). Inconsistent estimation and asymptotically equal interpolations in model-based geostatistics. Journal of the American Statistical Association, 99(465):250–261.